Nanoscale

Accepted Manuscript

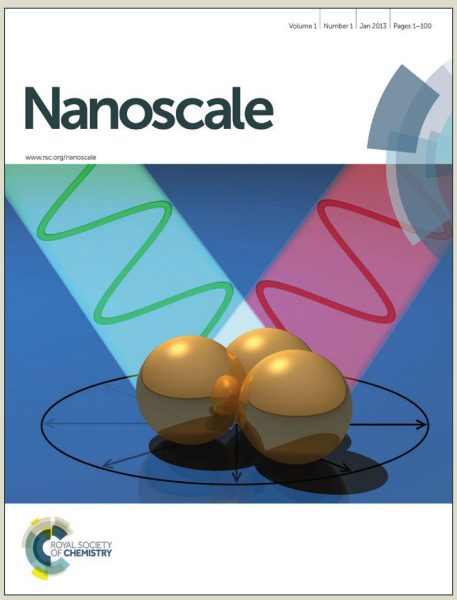

ROYAL SOCIETY OF CHEMISTRY

www.rsc.org/nanoscale

ARTICLE TYPE www. rsc.org/xxxxxx | XXXXXXXX

Tunable High Aspect Ratio Polymer Nanostructures for Cell Interfaces†

Kai Sandvold Beckwith*[a], Simon P. Cooil[a], Justin W. Wells[a] and Pawel Sikorski[a]

Received Xth XXXXXXXXXX 20XX, Accepted Xth XXXXXXXXX 20XX
First published on the web Xth XXXXXXXXXX 200X
DOI: 10.1039/b000000x

Nanoscale topographies and chemical patterns can be used as synthetic cell interfaces with a range of applications including study and control of cellular processes. Herein, we describe the fabrication of high aspect ratio nanostructures using electron beam lithography in the epoxy-based polymer SU-8. We show how nanostructure geometry, position and fluorescent properties can be tuned, allowing flexible device design. Further, thiol-epoxide reactions were developed to give effective and specific modification of SU-8 surface chemistry. SU-8 nanostructures were made directly on glass cover slips, enabling the use of high resolution optical techniques such as live-cell confocal, total internal reflection and 3D structured illumination microscopy to investigate cell interactions with the nanostructures. Details of cell adherence and spreading, plasma membrane conformation and actin organization in response to high aspect ratio nanopillars and nanolines were investigated. The versatile structural and chemical properties combined with high resolution cell imaging capabilities of this system are an important step towards better understanding and controlling cell interactions with nanomaterials.

Introduction

Analysing, perturbing and manipulating cells *in vitro* is of fundamental importance in unravelling the molecular mechanisms of life. In turn these insights can lead to better understanding and treatment of pathologies, as well as drive developments within fields such as tissue engineering and neuroscience. Adherent cells interact strongly with their surroundings and this interactivity can be exploited to study and modify cell behaviour by introducing topographical or chemical micro- and nanoscale features [1–5].

Recently, there have been significant developments in biological applications of nanostructured surfaces, in particular high aspect ratio nanowires, nanopillars and nanotubes [6,7].* In these systems, regular or randomly arranged nanostructures protrude vertically from a flat substrate. The geometry of the nanostructures allow them to form a cellular interface with a nanoscale cross-section (typically around 100 nm), while simultaneously protruding into the cell body, although the details of this interface is still an area of active research [8–10]. Biological use of high aspect ratio nanostructures has led to several novel applications, including electrical interrogation of neurons [11–13], single-cell force measurements [14], cell motility control [15–17], induction of stem cell differentiation [18], assessing differential cell response [19], cell capture [20,21] and nanostructure-aided delivery of various functional molecules [8,22–25].

So far, inorganic materials such as semiconductors with high stiffness (which translates into high potential aspect ratios) have been used in the design of high aspect ratio nanostructures for biological applications. However, there are several advantages in using polymer materials as nanostructured cell culture substrates [4,26,27]. These include low materials cost, rapid and mild processing, optical transparency for better readout and characterization possibilities, increased design flexibility, and biocompatibility. In this regard, SU-8 is a promising candidate material for realising high-aspect ratio nanostuctures in polymer materials. SU-8 is a photosensitive epoxy-based resin that is widely used in MEMS technologies for creating patterned microscale features of high aspect ratios due to its relatively high stiffness, chemical resistance, optical transparency and ease of processing [28]. To achieve nanoscale features, SU-8 has also been explored as an electron-beam resist, demonstrating very high electron sensitivity and sub-100 nm resolution for thin films [29]. Although the focus of most studies has been on low aspect ratio features, one group has demonstrated the use of 500 nm high SU-8 nanopillars for biosensing purposes [30,31], and nanoimprinted SU-8 nanopillars have also been used for cell traction force measurements [32].

In addition to the possibility of nanoscale patterning, SU-8 is chemically tunable and biocompatible [33,34]. SU-8 has

[a] *Department of Physics, Norwegian University of Science and Technology, Trondheim, Norway. E-mail: kai.beckwith@ntnu.no*

† Electronic Supplementary Information (ESI) available: See DOI: 10.1039/b000000x/

* Although there is no general consensus as to which dimensions constitute a high aspect ratio nanostructure, in a recent review on the field by Bonde et. al., [6], only nanostructures with a height above 500 nm and diameter below 500 nm were considered.

been functionalized via several different routes, including unreacted surface epoxide groups[35], epoxide ring-opening modification via treatment with strong oxidizing acids[34,36], photografting[37] or by exposure to oxygen plasma[38], in many cases followed by e.g. silane treatment[39]. For surface chemistry specific to SU-8, and therefore potentially orthogonal to other materials in the device, the unreacted epoxide groups offer the most attractive route for conjugation. Multifunctional amines are standard curatives for epoxy resins, and thus amine-epoxide reactions are well characterized[40]. However, for surface chemistry modification of SU-8, amine-based procedures have not been highly successful, with the few reported successes being time-consuming and harsh, increasing the likelihood of damaging fragile structures[35]. Thus novel approaches to specifically modify SU-8 surface chemistry are needed. Thiol-based chemistry offers an attractive alternative, as thiol-epoxide "click" reactions are gaining popularity as a simple and efficient conjugation method[41,42]. Indeed, thiol-modified oligonucleotides have been conjugated to SU-8 in a rapid UV-mediated "click" reaction[43], but this reactivity has not been explored in a more general sense.

In this work, we develop a flexible SU-8 based platform for biological applications, with emphasis on high aspect ratio nanostructures. We optimize the fabrication of up to 1 μm high SU-8 nanostructures by electron beam lithography directly on glass cover slips for facile integration with typical cell biology procedures and microscopy methods. Thiol-epoxide "click" reactions are implemented to selectively alter SU-8 surface chemistry. Further, cell responses to different high aspect ratio SU-8 nanostructures are investigated. In particular, we use methods such as high resolution live cell imaging and super-resolution microscopy for detailed characterization of the interface between cultured cells and SU-8 nanostructures. We show that the SU-8 nanostructures are highly cell compatible, but can influence cell shape, adhesion, membrane morphology and actin structure. The presented system offers promise for cell biological applications of high aspect ratio polymer nanostructures, while simultaneously allowing the investigation of the interface between the cells and nanostructures and subsequent cell responses to be studied in unprecedented detail.

Results and discussion

SU-8 nanostructure fabrication

High aspect ratio nanoscale features were defined in spin-coated SU-8 films on glass cover slips by electron beam lithography (Figure 1). Uniform arrays of nanopillars (Figure 1A and B) or nanolines (Figure 1C) could be made over mm^2-sized areas in under 5 minutes of exposure time. The fabrication was initially optimized by tuning electron exposure doses and process parameters including post-exposure baking and development to give nanostructures that withstood capillary collapse upon drying after development, while retaining as high aspect ratio as possible (details given in Materials and Methods). Using single pixel dots or lines as the exposure design, aspect ratios (height divided by feature width at half height) of about 7 could be obtained for the resulting nanoscale pillars and lines when 1 μm high, a doubling compared to previously reported results[30]. Tip diameters in this case were about 100-120 nm (see ESI† Figure S1).

Nanostructure height could be altered by spinning the initial SU-8 film to different thicknesses (Figure 1D). If thicker (i.e. $\geq$ 1 μm) SU-8 films were used, nanopillars and nanolines tapered outward toward their base due to electron scattering in the resist, limiting the height of well-defined nanoscale features to about 1 μm with our 30 kV electron beam lithography system (see ESI† Figure S2). Nanostructures could be arbitrarily patterned, the only limitation being that the spacing (array pitch) could not be less than approximately half the height of the SU-8 (i.e. 500 nm spacing for 1 μm high nanopillars), otherwise a rough, semi-continuous SU-8 layer was formed between features due to the proximity effect. Nanostructure diameter could be both reduced and increased from the diameter obtained by single-pixel exposure (Figure 1E). Increased feature diameters were obtained by exposing small areas rather than single pixels, to give arbitrary diameters above the initial 120 nm. To reduce nanostructure diameters, oxygen plasma etching was performed. A low power (50W) oxygen plasma controllably reduced both the height and diameter of the nanostructures. For 1 μm high nanopillars, the tip diameter could be reduced to about 50 nm with 2 minutes of oxygen plasma treatment, giving tip:height aspect ratios of over 16 after taking the reduced height into account (see ESI† Figure S1). The average aspect ratio remained similar to untreated nanopillars at about 7. 40-50 nm was a lower limit to the tip diameter using this method, as tips broke off and fragmented upon further etching.

Finally, the nanostructures could be made fluorescent by doping the SU-8 with a fluorescent dye (Figure 1E). Here, Rhodamine 6G (excitation at 561 nm) and Oxazine 170 (excitation at 633 nm) were used successfully, but any fluorescent dye could in principle be used as long as it is sufficiently hydrophobic to dissolve in the SU-8 solvent while retaining its fluorescent properties.

Direct writing using electron beam lithography is inherently a serial, and thus a "low" throughput technique. The advantages include high flexibility and the possibility to quickly alter designs, as well as having a simple process consisting of only very few processing steps. Further, positional accuracy, geometric control and optional intrinsic fluorescence give reliable and consistent results across experiments, and allow transfer of results to other systems. Even with a basic EBL

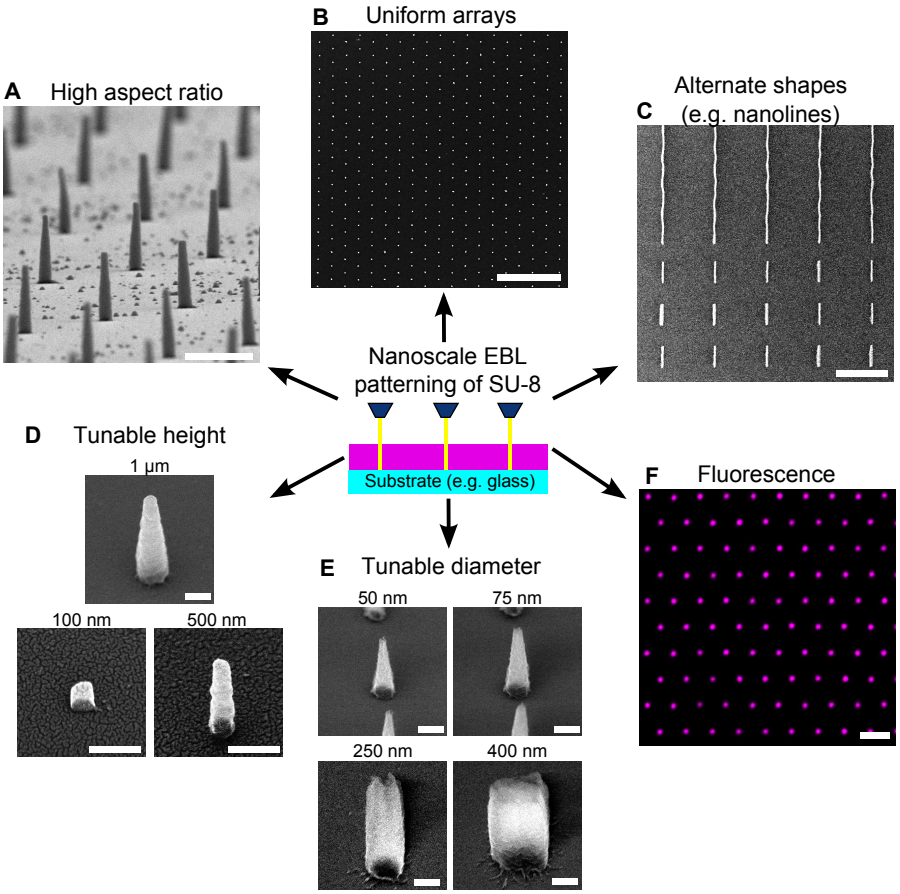

Fig. 1 Properties of high aspect ratio SU-8 nanostructures produced on glass cover slips by electron beam lithography. (A) Tilted SEM image of a regular hexagonal array of 1 µm high nanopillars with 5 µm spacing. Tip diameters are about 100-120 nm, and aspect ratio (height divided by average diameter) are about 7. Scale bar 1 µm. (B) Top view of hexagonal nanopillar array with 2 µm spacing. Scale bar 10 µm. (C) Top view of nanolines of different lengths (2 and 200 µm), with corresponding aspect ratios as the nanopillars. Scale bar 5 µm. (D) Nanostructure height was varied by using different SU-8 resist thicknesses, in the range of 100 nm to 1 µm. Scale bars 200 nm. (E) The diameter of nanostructures was altered compared to the initial single-pixel defined features, upwards by exposing larger areas and downwards by oxygen plasma etching for 60 s (75 nm tips) or 120 s (50 nm tips). Scale bar 200 nm. (F) Oxazine 170 or Rhodamine 6G-doped SU-8 was used to make fluorescent nanostructures, such as the hexagonal array (similar to (A) and (B)) shown in the confocal micrograph. Scale bar 2 µm. The SEM images in D and E are collected at 40° tilt from a top view, while (A) is collected at 85°.

system as the one used in this work, sufficient writing speed for laboratory-scale experiments (typically 1-2 minutes per mm^2) could be achieved due to the extreme sensitivity of the SU-8 resist[29]. Even this number would be greatly improved with modern, higher throughput EBL systems. One current limitation is the maximum feature height of about 1 µm, which is at the shorter end of the spectrum of high aspect ratio nanostructures reported in the literature[6]. However, EBL systems with higher acceleration voltages are available (typically 100-125 kV compared to 30 kV in our system), which would further increase the potential aspect ratio and height of the features[44], due to significantly lower electron scattering in the resist (see ESI† Figure S3). Other direct-write techniques such as direct laser writing (DLW) or two-photon polymerization could potentially increase device production throughput, but suffer from lower feature resolution[45,46]. Higher throughput, high resolution methods to structure SU-8 such as nanoimprint lithography[47] are attractive for further developments, while electron beam lithography offers simpler and faster prototyping for initial investigations.

SU-8 surface chemistry modifications

Simultaneous control over surface chemistry and surface topography is of great interest in biological applications. In particular, if the nanostructures are made of a different materials than the substrate, such as is the case of our SU-8 nanostructures on glass, new possibilities emerge for specifically tuning surface chemistry and cell response. To this end, we investigated the reactivity of unreacted epoxy-groups on SU-8 with candidate amino and thiol functional molecules under mild, aqueous conditions.

In particular, β-mercaptoethanol ($OH(CH_2)_2SH$, ME), 10 kDa PEG-thiol ($(CH_2CH_2O)_n-SH$, PEG-SH) and cysteamine ($NH_2(CH_2)_2SH$) were investigated as bi-functional thiols with different secondary groups. Ethanolamine ($OH(CH_2)_2NH_2$, EA) was used as a comparison as it is commonly used to quench epoxide groups[48]. Solutions were made at 1 M (except for PEG-SH which was made at 1 mM), and the pH was adjusted to the pKa of the reactive group (typically between pH=8 and pH=10) to ensure an equal concentration of the nucleophilic (deprotonated) species of each molecule. The surface modification potential of each molecule was initially assessed by measuring the static, advancing and receding water contact angles on uniform (unpatterned) SU-8 films after immersion in the modifying solution for up to 60 minutes at room temperature (Figure 2A).

The increased reactivity of the thiol species compared to similar amine species was demonstrated by the stronger reduction of contact angle observed for β-mercaptoethanol compared to ethanolamine. Another thiol, cysteamine, was investigated for introducing amine groups to the SU-8 surface, a key functionality for further biofunctionalization. Unexpectedly, cysteamine showed an extremely strong reduction of the water contact angle. Already after 15 minutes of incubation a strong contact angle reduction was observed, and after 60 minutes the SU-8 surface was nearly completely wetted by the test droplet (Figure 2B). This indicates a significant conversion of the epoxide groups to thioether-bound cysteamine. The reason for the increased efficacy of cysteamine compared to other thiol-species is unknown, but we speculate that it might be related to either an intra-molecular or inter-molecular catalytic effect of the amine group. For all surfaces a significant contact angle hysteresis (difference between advancing and receding contact angles) was observed, presumably reflecting the mixed surface chemistry present[49].

To verify that the negatively charged thiolate ions were indeed responsible for the modification of the SU-8 surface, additional experiments were performed with thiol-containing and control solutions at various pH and concentrations (see ESI† Figure S4). These indicate that 1 M cysteamine at alkaline pH was the most potent surface modification species, but also β-mercaptoethanol showed an increased effect at pKa compared to lower pH. Control solutions at high or low pH without amines or thiols only slightly altered the contact angle. As a positive control, freshly plasma cleaned SU-8 was observed to be completely wetting as previously described[38].

Further details of the wet chemical modification of SU-8 with cysteamine were investigated by x-ray photoelectron spectroscopy (XPS), a surface sensitive method. XPS analysis was performed of native SU-8 and cysteamine-modified SU-8 (1 hour incubation). Selective nitrogen 1s (Figure 2C) and sulphur 2p (Figure 2D) scans demonstrate increased nitrogen and sulphur content on the surface of the modified SU-8 films compared to native SU-8, indicating binding of cysteamine to SU-8. The increase in signal around 170 eV in the native SU-8 sulphur 2p spectra was attributed to a silicon 2p plasmon loss peak from the underlying substrate through defects or scratches in the SU-8 film (see also ESI† Figure S5). Peak area quantification of the cysteamine-modified SU-8 spectrum yielded normalized atomic percentages for carbon 1s (60%), oxygen 1s (37%), nitrogen 1s (2%) and sulphur 2p (1%), a nitrogen/carbon ratio of 0.03 and a sulphur/carbon ratio of 0.013. As each cysteamine molecule contains one nitrogen and one sulphur, the increased signal of nitrogen compared to sulphur indicates that it is the thiol group of cysteamine that binds to SU-8, as indicated in the contact angle studies. Although the atomic percentages apparently indicate a quite low coverage of cysteamine on SU-8, cysteamine monolayers on gold are known to absorb significant amounts of oxygen- and carbon-containing contaminating molecules. In one study, even at full monolayer coverage of cysteamine, the nitrogen/carbon ratio was only 0.1 compared to the theoretical value of about 0.5[50]. In our case the underlying surface (SU-8)

also consists of carbon and oxygen, and it was not possible to distinguish the carbon and oxygen contribution from surface contamination and the SU-8. Quantification of the cysteamine surface coverage was therefore not possible, but the surface coverage is likely significantly higher than indicated by the atomic percentages.

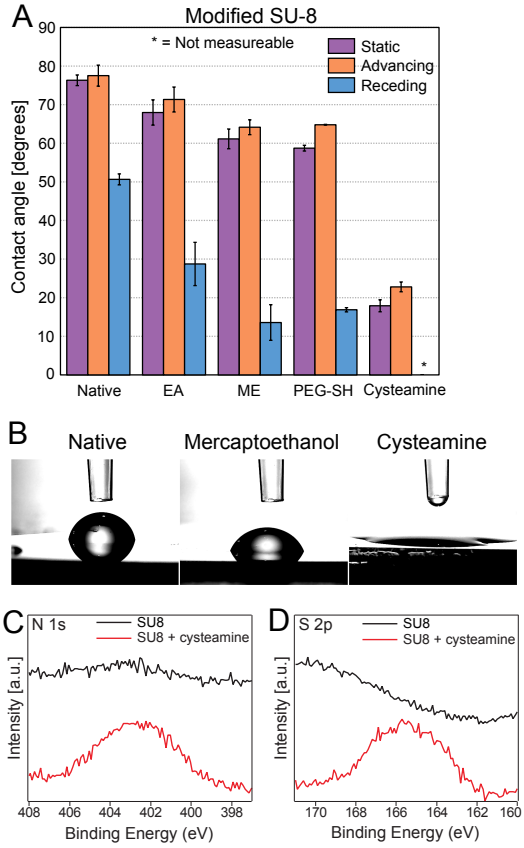

Fig. 2 (A) Static, advancing and receding contact angle of SU-8 after reacting surface-epoxide groups with ethanolamine (EA), β-mercapto ethanol (ME), PEG-thiol and cysteamine. All treatments were 1 hour at room temperature, except cysteamine which was 15 minutes, as 60 minutes of cysteamine gave non-measureable ($< 10^{\circ}$) contact angles. Error bars indicate $\pm$ S.D. (B) Examples of images acquired during contact angle measurements, illustrating the changes in contact angles that occurred. High resolution XPS spectra of nitrogen 1s (C) and sulphur 2p (D) peaks of native and cysteamine-modified SU-8.

To demonstrate the chemical functionality of modified SU-8 surfaces, fluorescent NHS-rhodamine was used as a probe (Figure 3A). NHS-rhodamine binds covalently to amine groups, such as those introduced by the cysteamine reaction with unreacted SU-8 epoxide groups. Conversely, due to its inherent hydrophobicity, native SU-8 is known to have high non-specific adsorption[46], so other treatments were assessed to reduce non-specific adsorption of NHS-rhodamine to SU-8. Under the measurement conditions, some SU-8 autofluorescence was observed, constituting the signal in the unlabelled control. As expected, untreated SU-8 showed an increased fluorescence signal after treatment with NHS-rhodamine due to non-specific adsorption. Treatment of SU-8 with oxygen plasma, β-mercaptoethanol or PEG-SH reduced NHS-rhodamine binding to SU-8 to levels close to the unlabelled control. In comparison, cysteamine-treated SU-8 showed a substantial increase in fluorescence signal, indicating conjugation of NHS-rhodamine to the amine groups presented by the cysteamine-modified SU-8. It should be noted that during initial experiments it was observed that the chemistry of the glass substrate was altered after the SU-8 fabrication process, leading to an observable fluorescent background on the glass after NHS-rhodamine treatment. To regenerate the expected surface chemistry of glass, a NaOH-based wet chemical cleaning step was implemented for all experiments, as this cleaning method did not appear to alter SU-8 chemistry (see details in ESI†).

"Orthogonal" chemistry, i.e. introduction of independent functionality on SU-8 and glass, was demonstrated by specifically labelling the glass substrate after treatment of patterned SU-8 features with cysteamine and NHS-rhodamine (Figure 3B). The glass was labelled with FITC-labelled poly(ethyleneimine) (PEI), which is a highly cationic polymer that binds strongly to the negatively charged glass. Conversely, PEI would not bind to the rhodamine-modified SU-8. Using this method, both larger SU-8 features and SU-8 nanopillars were selectively labelled with NHS-rhodamine, while the glass was selectively labelled with FITC-PEI.

Orthogonal modification could be used to tune cell adhesion properties to glass or SU-8. As PEG monolayers are well known for preventing cell adhesion, SU-8 was modified by PEG-SH to see if a reduction in cell adhesion was obtained. Although the standard modification procedure used above reduced the contact angle and NHS-rhodamine binding on SU-8, the PEG-layer formed was presumably not dense enough to significantly reduce cell adhesion, as little difference was observed compared to control samples. To increase the PEG-SH-epoxide reaction efficiency, UV-light was used to catalyse the reaction, as recently described for immobilizing thiolated DNA oligomers[43,51]. The UV-immobilized PEG-SH monolayer on SU-8 substantially reduced cell adhesion to SU-8 features, while cell adhesion was still supported on the surrounding glass areas (Figure 3C).

Conversely, to avoid cell adhesion on glass, while allowing cells to attach to SU-8 features, the samples were cleaned as above and incubated in PLL-g-PEG, which creates a cell-repellent self-assembled monolayer on negatively charged surfaces[52]. After cell culturing, almost no cells adhered on the glass, while adhering well to the unmodified SU-8 (Figure 3D).

It is possible that other solution conditions such as increased pH or temperature or the inclusions of catalysts could increase the efficiency of the thiol-based SU-8 modification reactions. However, we have shown that even at mildly alkaline aqueous conditions the thiol-based solutions are potent at modifying SU-8 micro- and nanostructures, especially in the case of cysteamine forming an amine-rich surface on the SU-8. UV-enhanced grafting offers an alternative route that increases grafting efficiency, such as in the case of directly rendering SU-8 cell repellent by PEG-SH treatment. Such simple and robust surface modifications can have great impact for the use of SU-8 in e.g. DNA microarrays[34], microfluidics[35] or for cell device applications[39] as also presented here.

General influences of SU-8 nanostructures on cells

Cell compatibility, ease of use and high quality imaging are advantageous features of nanostructured devices when used for cell biological applications. Standard glass cover slips patterned with SU-8 nanostructures were mounted under 3.5 mm holes drilled in the base of 35 mm petri dishes, in a configuration similar to standard glass-bottom dishes used for microscopy (see schematic in ESI† Figure S6). To reduce the number of variables investigated, only oxygen plasma treated nanostructures were used for cell investigations, ensuring a highly cell-compatible surface chemistry[53]. Unless otherwise specified, 1 µm high nanostructures in hexagonal arrays were used for all experiments.

To assess cell-nanostructure compatibility, HeLa cells were grown on nanopillars and nanolines 1 µm high and 120 nm in diameter with different spacings for 24 hours, stained with live/dead staining (calcein-AM and propidium iodide) and imaged live using confocal microscopy. Images were automatically analysed using CellProfiler. For all nanopillar spacings, the viability was about 98%, similar to glass controls (Figure 4A), and cell density was also unchanged at about 400 cells/mm^2 for the chosen seeding density (20 000 cells/cm^2). A reduction in projected spreading area of the cells was observed for nanopillars spaced by 0.75 µm to 2 µm, while for nanopillars spaced by 5 µm the spreading area was not significantly different from glass controls. At the measured cell areas, 1 µm and 5 µm spacing correspond to about 500 and 30 nanopillars per cell, respectively. High viability but somewhat reduced spreading area is consistent with earlier reports of cells on e.g. polystyrene nanopillars of similar dimensions as ours (although more densely spaced)[54], and also general trends in studies of cells on other types of high aspect ratio nanostructures[6].

In addition, it was investigated whether nanolines could induce directional effects in the cells (i.e. elongation and orientation alignment), as it is well known that cells tend to align along elongated topography in the substrate[55]. Indeed, on

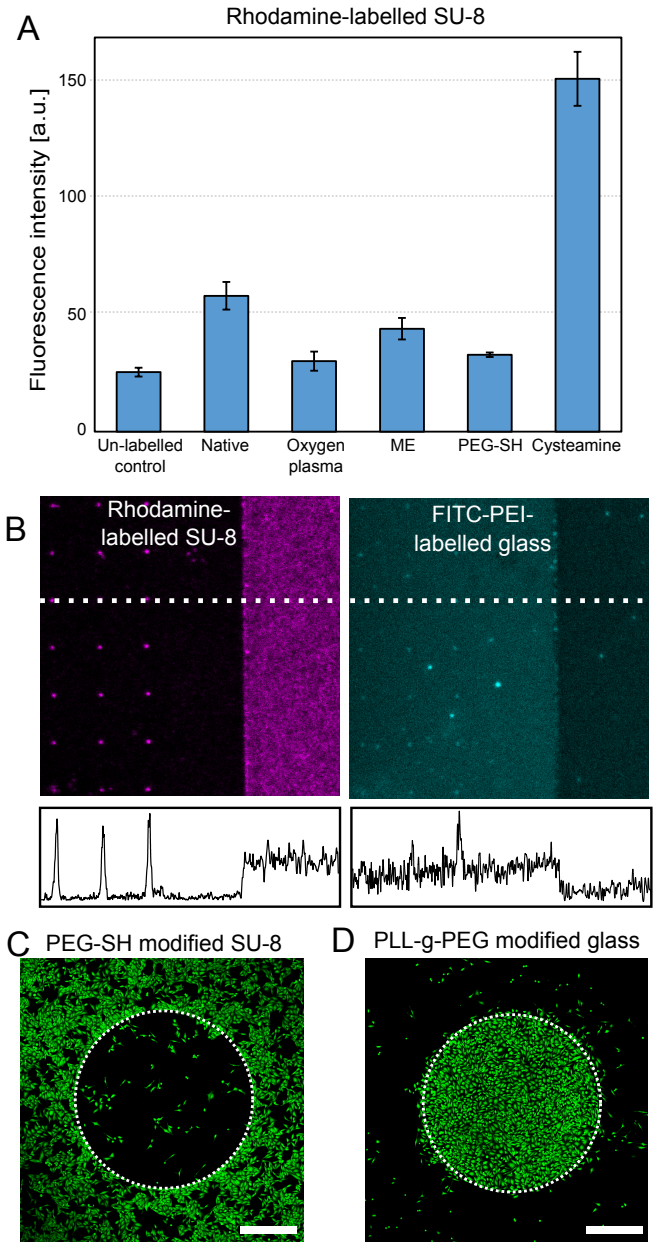

Fig. 3 (A) Fluorescence intensity of flat SU-8 surfaces labelled by NHS-rhodamine after various surface treatments. The signal in the negative control is SU-8 autofluorescence. Error bars indicate ± S.D. (B) Orthogonal labelling of SU-8 and glass. SU-8 was functionalized with cysteamine and conjugated to NHS-rhodamine, while the negatively charged glass was subsequently labelled by FITC-PEI. Below each figure are intensity linescans from the indicated dashed lines. (C, D) Calcein-AM-labelled HeLa cells grown on large-scale SU-8 features on glass. When modified with PEG-SH (C), the cell adhesion was reduced on SU-8 features. When the glass was modified by PLL-g-PEG (D), cell adhesion was instead reduced on glass, while the unmodified SU-8 was able to support cell adhesion. The SU-8 area is delineated by the stippled circle, the scale bar is 500 µm.

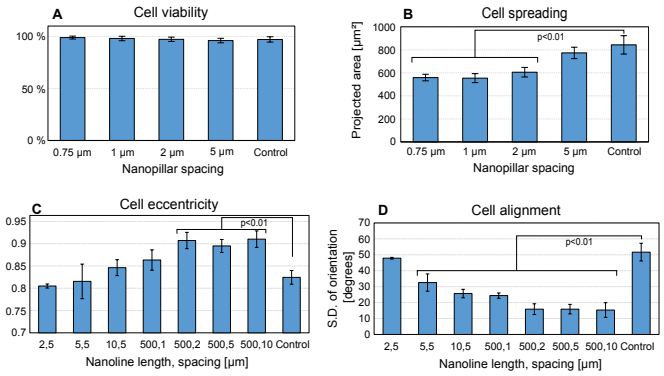

Fig. 4 HeLa cells were cultured for 24 hours on substrates with 1 µm high, 120 nm diameter oxygen plasma treated hexagonal SU-8 nanopillar arrays with nanopillar spacings of 0.75 µm to 5 µm, or square nanoline arrays with 1 µm high, 120 nm diameter nanolines with lenghts of 2 µm to 500 µm and spacings of 1 µm to 10 µm and compared to glass controls. The cells were labelled with calcein-AM (live cells) and propidium iodide (dead cells) and imaged live using a 10X objective and analysed for viability and cell shape using CellProfiler. (A) Cell viability was unchanged from glass controls for the different nanopillar spacings. (B) Projected cell area was significantly reduced on nanopillar array spacings of 0.75 µm to 2 µm, while the area was similar to flat glass for 5 µm spaced nanopillar arrays. (C) Cells became more elongated and (D) better aligned compared to glass controls on nanolines, especially longer nanolines. Error bars indicate ±S.D., significance assessed by student's t-test, 2-tailed assuming unequal variance.

nanolines 1 µm high, with a top diameter of about 120 nm, spacings of 1-10µm and lengths from 2 µm to 500 µm, both elongation and alignment of cell orientation with the nanolines was observed (Figure 4C and D). Elongation was measured by the ratio of the major axis to minor axis of the best-fit ellipse for each cell, while alignment was measured by the standard deviation in the orientation of the major axis of the ellipse. In particular, nanolines substantially longer than the cells (i.e. 500 µm) gave the strongest elongation and alignment, although 5 and 10 µm lines also gave a stronger alignment than 2 µm lines or glass control. On the other hand, for 500 µm long lines the spacing was less important in the investigated range, except in the case of 1 µm, where both elongation and alignment was reduced. The high degree of tunability and control over elongated high aspect ratio features can have important applications within neural studies and *in vitro* neural network construction[45].

Cell interactions with SU-8 nanostructures

To gain a better understanding of how single cells respond to the SU-8 nanostructures, in particular 1 µm high nanopillars and nanolines, high resolution optical microscopy was used to image HeLa cell cytoplasm, plasma membrane and actin filaments while growing on nanostructures. The cells were studied 24 hours after seeding, to ensure that all initial cell adherence processes had completed. For initial investigations, the cell cytoplasm was labelled with calcein-AM, and the cells were imaged live using a 63X 1.4NA oil immersion objective. As has been reported before for nanowires[8,22], the nanostructures were visible as black features (dots or lines) against the fluorecent cell cytoplasm due to the cytoplasmic volume excluded by the nanopillars (Figure 5). One noticeable feature was that cells on nanopillars spaced by ≤ 1 µm in many cases had a reduced cytoplasmic signal in significant portions of the cell body (Figure 5A). This can be explained by a "bed of nail" effect, where areas of the cell body were suspended above the cover slip (and thus above the focal volume of the microscope), appearing darker. This situation was dynamic, as the area of the cell body in contact with the cover slip changed over time, as shown in excerpts from a one hour time-lapse in Figure 5A. The full time-lapse is available in ESI† Movie S1. The opposite case, where initially adhered areas of a cell became suspended, was also observed (ESI† Movie S1). The occurrence of a number of mobile filopodial extensions was observed under the suspended areas of the cell.

Such a "bed-of-nails" effect on cells suspended by dense arrays of high aspect ratio nanostructures has been reported before[9,56], but in these cases the nanowires were longer than our nanopillars (typically 5-10 µm compared to 1 µm), leading in most cases to suspension of the entire cell body (occasionally excluding longer protrusions such as axons). In contrast, we observed that in all cases at least a portion of the cell body remained in contact with the cover slip. Even "fully adhered" cells, typically observed on nanopillars spaced by ≥ 2 µm, the height of the cytoplasm (and thus the contact with the cover slip) could also fluctuate in an area around the position of single nanopillars, as indicated by a temporarily reduction in the cytoplasmic signal (Figure 5B). This can be envisioned as a the cell cytoplasms adopting a tent-shaped surface with the nanopillar as the tent-pole. This form of local cell cytoplasm deformation has been described theoretically[57], and these results indicate demonstrate these states as part of a dynamic interaction between the cells and nanopillars.

Shorter nanolines (2 µm long and spaced by 2 µm) caused a similar cytoplasm exclusion effect as nanopillars at all line positions (Figure 5C), while longer lines (e.g. 500 µm spaced by 2 µm) additionally suspended larger areas of the cells, as indicated by darker areas in the cell cytoplasm (Figure 5D).

Together, these results indicate that there is a constant and shifting balance of forces between adhesion energy to the cover slip (and possibly the nanostructures) on one hand, and the energy required to engulf the nanostructures on the other hand, as also indicated by theoretical models[57]. These changes in modes of cell adhesions could have implications

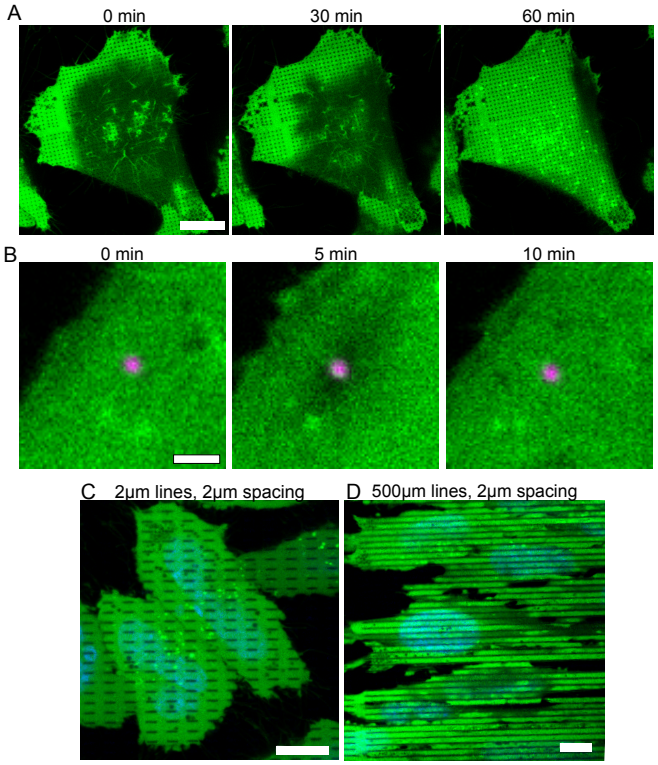

Fig. 5 Confocal micrographs of live calcein-AM labelled (green) HeLa cells showing dynamics of cell adhesion on nanopillar substrates. The focal plane was fixed just above the substrate, brighter areas indicate cell cytoplasm close to the coverslip, darker areas indicate cell cytoplasm raised from the coverslip. (A) Single HeLa cell transitioning from a mostly suspended to nearly fully adhered state on 1 µm spaced nanopillars. Nanopillars are seen as black dots against the green cytoplasmic background. Scale bar 10 µm. (B) Cells were generally adhered on 5 µm spaced nanopillars, but the cell cytoplasm distance to the cover slip could still fluctuate locally around single nanopillars as observed by a temporary decrease of the intensity. An image of the nanopillar (magenta dot) is overlayed. Scale bar 2 µm. The full time-lapse sequences are available in the ESI† as Movie S1 and S2. (C) On shorter lines, such as 2 µm lines spaced by 2 µm, the cells remained fully adhered, only showing a cytoplasmic exclusion effect at the nanolines, while on longer lines of 500 µm spaced by 2 µm (D), larger areas of the cells could be suspended between the lines, as seen by the darker cytoplasmic signal in portions of the cells. Scale bars (C) and (D) are 10 µm, Hoechst-labelled nucleus shown in cyan.

for applications within cell migration[15], cell force studies[14], as well as cell capture[58] and stem cell guidance[27].

Although the cytoplasmic exclusion effect is occasionally indicated as proof of cell plasma membrane penetration, we and others have shown that the cell plasma membrane can wrap tightly around high aspect ratio nanostructures, leading to similar cytoplasmic images without membrane penetration[8,10,59]. To gain increased insight into the cell membrane conformation around our SU-8 nanopillars, in particular to investigate whether nanopillars could be observed to penetrate the cell plasma membrane, we used combined widefield and TIRF fluorescence imaging of CellMask Orange-labelled HeLa cells (Figure 6).

On square arrays of 1 µm high, 120 nm tip diameter nanopillar arrays spaced by 1 µm, an increased membrane signal was observed at each nanopillar site, although the signal varied within each cell (Figure 6A, left panel). This effect can be explained by considering that if the cell membrane wraps around the nanopillar, the number of fluorophores in the fluorescence excitation volume (which typically extends at least 500 nm in z-direction) increases as the membrane rises along the nanopillars in parallel with the optical axis[60]. The signal intensity variation can be explained by different degrees of cell membrane wrapping around the nanopillars, as the cell is suspended to various heights. Correspondingly, as TIRF microscopy is only sensitive to fluorescent structures within close vicinity (50-100 nm) of the cover slip, adhered areas of the cell membrane gave a strong signal, while in areas where the cell membrane was suspended by the nanopillars the TIRF signal disappeared (Figure 6A, center panel). This occurred both locally at each nanopillar, and over larger areas towards the cell centers, confirming the results from the cell cytoplasm imaging above. The cell body suspension effect disappeared as soon as the spacing between the nanopillars increased, even locally, as could be observed at the gap in the nanopillar pattern indicated in Figure 6A. On 2 µm spaced pillars, the cells remained fully adhered as indicated by the corresponding TIRF and widefield signals (ESI† Figure S7).

By comparing the relative intensities of the widefield and TIRF signals, three observed membrane states are proposed (Figure 6B). State (1), with a strong TIRF signal adjacent to the nanopillars and the widefield membrane signal enhanced at the nanopillar site, indicates a tight wrapping of the nanopillar by the cell membrane. In state (2), the absence of a TIRF signal indicates that the membrane is suspended, and the reduced widefield signal indicates a low degree of nanopillar wrapping. In state (3), the presence of a increased widefield signal combined with the absence of a TIRF signal indicates partial membrane wrapping of the nanopillars, and thus is an intermediate state between fully wrapping (1) and suspended (2) states.

A fourth state is also possible, in which the nanopillars

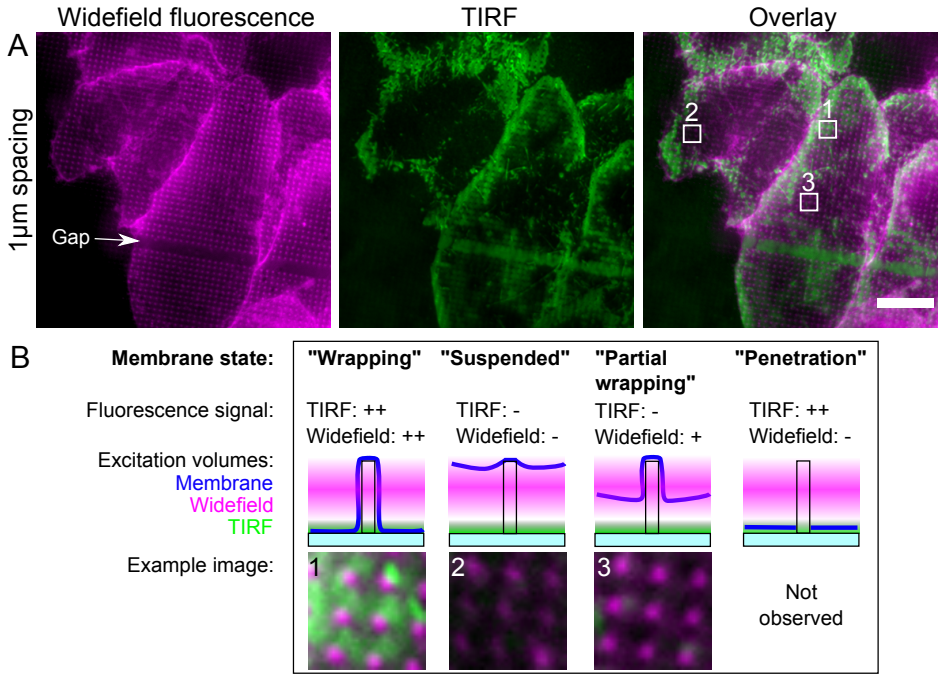

Fig. 6 Widefield and TIRF micrographs of the plasma membrane of CellMask orange-labelled HeLa cells on 1 µm high square nanopillar arrays with 1 µm spacing. (A) An increase of widefield signal could be observed at nanopillar locations (left panel), although in general the membrane signal was stronger towards the periphery of the cells. Corresponding TIRF images (center panel) highlights areas of the cell membrane in contact with the cover slip, demonstrating that the cell membrane is in fact suspended towards the center of the cells on this nanopillar spacing. Gaps in the nanopillar array such as indicated in the left panel led to membrane contact with the cover slip. (B) By inspection of the intensity relations between widefield and TIRF signals of the same areas, several alternate membrane states are proposed. (1) Fully ”wrapping”, (2) fully ”suspended” or (3) ”partial wrapping”, taken from the areas marked in (A). The fourth alternative state of ”penetration” was not observed. Scale bars 5 µm.

would directly penetrate the cell membrane and no wrapping would occur. This state would be characterized by a low wide-field signal together with a high TIRF signal, but this was not observed in our experiments. Transmission electron microscopy (TEM) investigations of neurons on quartz nanopillar arrays have revealed similar results, indicating both wrapping and suspended states, depending on nanopillar diameter and spacing[10]. However, the interim states of partial wrapping of nanopillars, or that different areas of the cell is suspended or adhered to the cover slip was not reported, and would be beneficial to investigate further using TEM. Note that a local membrane penetration only at the top of the nanopillar or at isolated places along the nanopillar could still occur as suggested in theoretical models[57], as this state would not be distinguishable from state (1) or (3).

Actin filaments and cell membrane dynamics are highly interrelated[61]. Previous observations indicate that actin filaments might be influenced by the presence of high aspect ratio nanostructures[8]. This was observed to be the case for our SU-8 nanopillars and nanolines as well. Initial confocal microscopy showed colocalization between phallodin-labelled actin in HeLa cells and nanopillars, but the resolution was insufficient to gain further insight into the actin structure (see ESI† Figure S8). Due to the nature of our device (the 0.17 mm glass cover slip substrate in particular) super-resolution optical microscopy methods such as 3D-SIM and STED could be used to image actin filaments at higher resolution. Actin was observed to bundle around the nanopillars, although the amount of actin varied from pillar to pillar (Figure 7A). Thus, it is unlikely that this effect arises only due to signal enhancement as described for the membrane signal above, rather a more specific interaction is likely in this case. Additionally, in certain cells (about 10%) on 1 μm spaced nanopillars, alignment of actin filaments was observed along specific directions in the nanopillar array (a hexagonal array in this case), as shown in Figure 7B. On 500 μm nanolines, which were shown to induce the strongest alignment and elongation above, regular confocal microscopy showed alignment of the actin filaments along the direction of the nanolines (Figure 7C). The actin filaments did not appear to bind to the nanolines, but rather formed between them, although actin filaments were observed to cross lines occasionally (figure 7C, inset). Finally, 500 μm nanolines could be seen to induce the formation of highly elongated, actin-containing cell protrusions (up to 200 μm in length), which were guided along the sides of single nanolines (Figure 7D).

Although filopodia are known to react and bind to nanoscale topographies[62], such local and specific actin structures have not been reported before on high aspect ratio nanostructures, and could contribute in the understanding cell interactions with nanostructured surfaces.

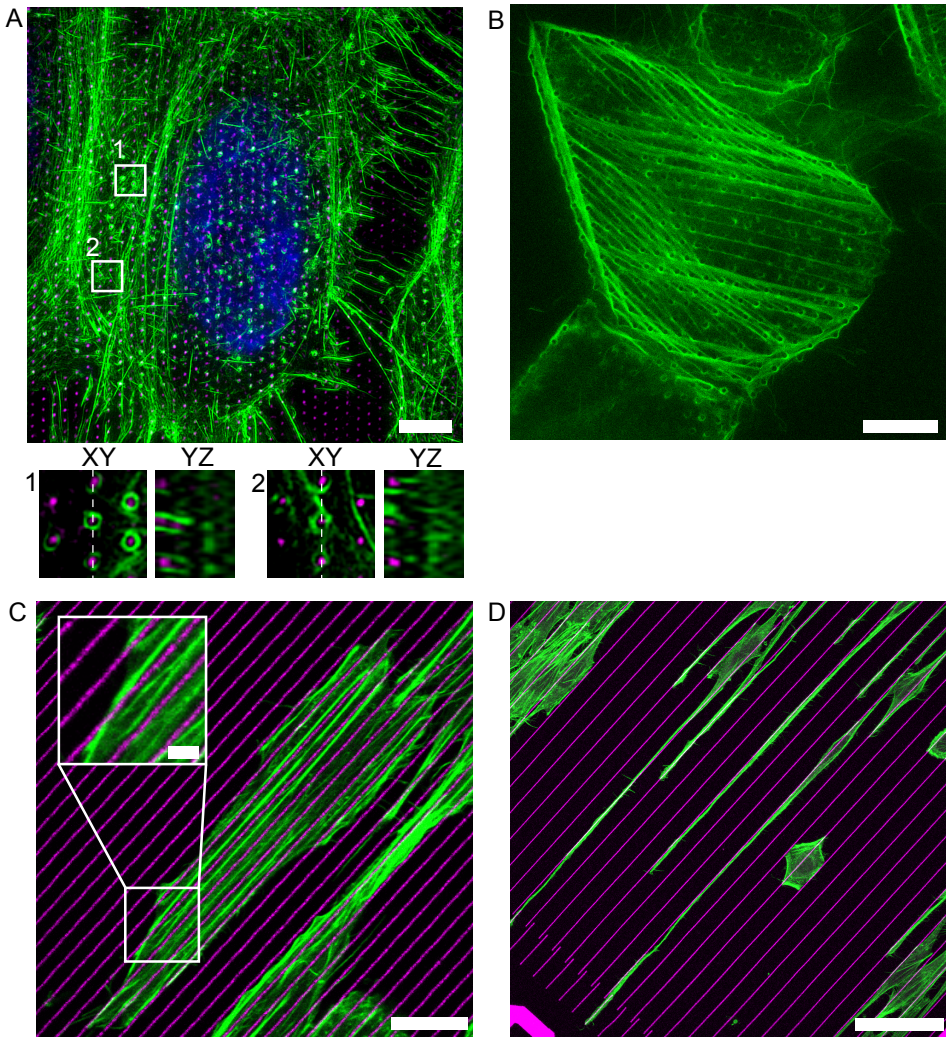

Fig. 7 3D-SIM, STED and confocal microscopy of HeLa cell actin in response to arrays of 1 μm high, 120 nm diameter nanopillars and nanolines. Maximum intensity projection of a 3D-SIM stack showing phalloidin-Alexa488-labelled actin (green), Hoechst 34580 labelled nucleus (blue) and 1 μm spaced nanopillars (magenta) in a hexagonal array. The actin filaments associated with the nanopillars at multiple locations both in the cell center and periphery. The cut-outs are single planes and cross-sections from the stack at the indicated positions. Scale bar 5 μm. (B) STED image of actin filaments forming aligned bundles that appear to be directed by the the hexagonal array of nanopillars in the majority of the cell. (C) Confocal micrograph of cells on 1 μm high, 500 μm long nanolines spaced by 2 μm, showing that actin filaments orient along the direction of the nanolines, but do not appear to bind significantly to the nanolines. However, actin filaments could cross the nanolines, as shown in the inset. Scale bar 10 μm, inset 2 μm. (D) 500 μm long nanolines spaced by 10 μm could guide actin-containing cellular protrusions along the side of the lines, leading to highly elongated cells spanning up to 400 μm. Scale bar 50 μm.

Conclusion

Enhanced surface-based delivery of functional biomolecules[23,24,63], neural guidance[15,56], cell differentiation and response[18,19] and circulating tumour cell capture[21] are some examples of interesting applications of high aspect ratio nanostructures, and further developments rely on a better understanding of the fundamental interactions between cells and nanostructures. In this work we have developed a flexible nanostructured polymer-based system optimized for cell biology applications and investigations. Our results demonstrate strong interactions between cells and high aspect ratio polymer nanostructures, influencing several aspects of cell response. Due to the design of our system, where the nanostructures were produced directly on standard glass cover-slips, super-resolution microscopy methods such as TIRF, STED and 3D-SIM together with live-cell imaging revealed details about how the actin cytoskeleton and cell membrane conform to and bind to the nanostuctures, giving important indications of the underlying mechanisms of cell responses. In particular, detailed views of actin associating with nanopillars, actin fiber guidance by nanolines, cell membrane wrapping of nanopillars and the dynamics of cell adherence on the nanopillars demonstrate the range of little characterized biological responses to high aspect ratio nanostructures that were investigated in the presented system. In addition, due to the flexibility of the single-step patterning and fabrication approach together with high control over nanostructure surface chemistry, the range of tunable parameters greatly increases, allowing us to e.g. explore the effects of nanolines compared to nanopillars. However, here we only investigated a small subset of the available parameter space offered by the presented fabrication and chemical modification processes. Although we focus on high aspect ratio nanostructures, the introduced platform can be extended to other types of nano-scale patterns. A range of further parameters, especially independent tuning of nanostructure geometry and surface chemistry, should be further investigated for their influence on the structure and functionality of different cell types. Through the use of systems that are controllable yet flexible, one can start to unravel the causal relationships between membrane dynamics, cytoskeletal arrangements, and functional cell responses that lead to novel biotechnological applications.

Materials and Methods

SU-8 nanostructure fabrication

All chemicals and reagents were purchased for Sigma-Aldrich (Oslo, Norway) unless otherwise specified.

0.17 mm (# 1.5) glass cover slips (Menzel-Glaser borosilicate glass) were cleaned in acetone, isopropanol and DIW, then subjected to oxygen plasma of 0.8 mbar at 100 W for 2 minutes in a Diener Femto plasma cleaner. The glass was then rinsed again in acetone, isopropanol and DIW, dehydrated for 2 minutes on a 95 °C hot plate, before spin coating SU-8.

To produce SU-8 solutions of different viscosities (and therefore final film thickness), SU-8 2100 (Microchem) was diluted in SU-8 2000 thinner (cyclopentanone, Microchem). Fluorescent SU-8 was made by mixing the SU-8 with the hydrophobic laser dyes Rhodamine 6G or Oxazine 170. The dyes were dissolved directly in the SU-8 resist to a final concentration of 100 µg mL^{-1}. SU-8 was spin coated at 6000 rpm for 36 s to produce SU-8 layers of the desired thickness (from 100-2000 nm). The samples were then soft-baked for 1 minute at 95 °C.

Electron beam exposure of the SU-8 was performed in a Hitachi S-4300 SEM modified with a Raith Quantum stage and pattern generator. The exposures were performed at 30 kV with a 100 pA beam current. The exposure dose was varied to find the optimal exposures as described in the main text. Nanopillars and nanolines were typically exposed as single-pixel dots or lines, but larger areas could be written to achieve larger features. Optimized exposure doses for different feature types are detailed in the electronic supplementary information (ESI†). The samples were then post-exposure baked at 95 °C for 1 minute, developed with mild agitation for 20 s in SU-8 developer (mr-dev 600, Microchem), 20 s in fresh developer then rinsed in isopropanol and dried with N_2. Longer post-exposure bakes (2-5 minutes) were possible, and lead to nanostructures with increased diameter but also increased stability during handling. Oxygen plasma thinning of the nanopillars was performed for 30-210 s in a 0.4 mbar oxygen plasma at 50W.

Finished devices were scribed using a Dynatex DX-III scriber into small samples (typically 6x6 mm). The samples were imaged using a Hitachi S-4300 or Hitachi S-5500 SEM after sputter coating a 5 nm Au layer for observation, and a Leica SP5 confocal microscope with the appropriate laser lines (561 nm for Rhodamine6G, 633 nm for Oxazine 170). During SEM imaging the samples were tilted to 40° or 85° for observation of standing nanopillars. Electron trajectory simulations were performed using Casino v. 2.48[64].

Unless specifically modified as described below, samples for cell culturing were typically treated with oxygen plasma at 0.4 mbar at 50 W for 30 s.

SU-8 surface modification and surface characterization

Wet chemical surface modification of SU-8 was performed by incubating test surfaces in aqueous solutions containing molecules with thiol or amine groups. The SU-8 test surfaces were made as above, but instead of electron-beam lithography

exposure, the SU-8 was flood-exposed or exposed through a quartz-chrome mask with 365 nm UV light 500 mJ cm^{-2} in a Carl Suss MA6 mask aligner. Surfaces patterned by electron beam lithography where tested in the last step of the method development process. During initial experiments, a contaminating layer was observed on the glass surface after SU-8 processing (unless oxygen plasma treatment was used). Thus a cleaning step was implemented prior to surface modification: The sample was immersed for 1 minute in 1 M NaOH in milliQ water at 50 °C.

The pH of each modification solution was set to the pKa of the active thiolate or amine species. Solutions of 1 M of ethanolamine (pH=9.50), cysteamine (pH=8.2), β-mercaptoethanol (pH=9.64), and a 1 mM solution of O-(2-Mercaptoethyl)-O-methylpolyethylene glycol (PEG-SH, molecular weight 10kDa, pKa not available but assumed to be similar to 3-methyl mercaptoproprionate at pH=9.33) were made in milliQ water and the pH was set by addition of 1 M HCl or 1 M NaOH, or 10 mM bicarbonate in the case of PEG-SH. Working solutions were freshly made to avoid auto-oxidation of the thiol species[65]. To increase the shelf life of stock thiol-containing solutions, 1 mM of EDTA was added, and the pH was left at the native pH of the solutions before adding NaOH, reducing the number of active thiolate species to a minimum. Just before use, the appropriate amount of 1 M NaOH was added to increase the pH to the value given above. After incubating the samples for a certain reaction time (typically 60 minutes) at room temperature, the surfaces were rinsed thoroughly in milliQ water and dried using compressed air.

To assess the efficacy of the various modification solutions, contact angles were measured on the modified SU-8 surfaces. 2 µL droplets were dispensed and static, advancing and receding contact angles were measured using an in-house made contact angle measuring apparatus. The contact angle images were analysed using the LB-ADSA part of the Droplet Analysis plugin[66] for FIJI[67]. At least three samples per condition were measured.

X-ray photoelectron spectroscopy (XPS) measurements were performed using a Specs PHOIBOS-150 hemispherical electron analyser and MgK_α X-ray lamp (h_ν = 1253.6 eV) connected to a custom UHV system with base pressure of 1E-10 mbar. Survey scans were collected at E_{pass} = 150 eV and E_{step} = 1 eV, and selected regions (N 1s and S 2p) were captured for the same pass energy and E_{step} = 0.1eV. Silicon wafers with 500 nm SU-8 films, native or modified for 1 hour with cysteamine as described above, were washed in ethanol in a ultrasonic bath and then blown dry with N2 gas before being introduced into the vacuum system.

To verify the functionality of the surfaces, SU-8 features prepared by UV-lithography or electron beam lithography and modified according to the procedures above were labelled using the amine-reactive NHS-rhodamine. 1 µM NHS-rhodamine in 10 mM HEPES, pH=8.0 was incubated for 1 hour on each sample, and the samples were rinsed thoroughly in ethanol and milliQ water before imaging. The fluorescent intensity was measured using 561 nm excitation and 580-650 nm emission on a Leica SP5 confocal microscope, at least three samples per condition were measured.

Finally, SU-8 and glass were independently modified and labelled. For fluorescence visualization experiments, the SU-8 was first modified by cysteamine and labelled with NHS-rhodamine and cleaned as described above, then the glass was labelled with 1 mg ml^{-1} FITC-labelled poly(ethylene imine) in milliQ water for 1 hour, prepared as described previously[68].

For differential cell adhesion experiments two modification schemes were employed. To repel cell attachment from glass while allowing cell attachment to SU-8 features, the samples were incubated in 0.1 mg ml^{-1} PLL(20kDa)-g-PEG(5kDa) (Susos AG, Dübendorf, Switzerland) in 10 mM HEPES, pH=7.4 at room temperature for 1 hour[69]. To repel cell attachment from the SU-8 features while allowing cell attachment on glass, the samples were incubated in 1 mM SH-PEG in 10 mM bicarbonate, pH=9.33. The last incubation was performed under UV illumination from a Dymax Bluewave 50 UV lamp for 15 minutes (approximate illumination intensity of 30 mW cm^{-2})[43].

Cell experiments

For cell experiments, a simple procedure was used to integrate the nanostructured samples into suitable cell culturing dishes: 3.5 mm holes were drilled into the base of 35 mm polystyrene petri dishes (Nucleon, tissue culture treated). Subsequently, the sample was adhered underneath the petri dish with a thin layer of liquid paraffin. As the paraffin solidified, a robust, water-tight seal was formed, with the SU-8 features on glass in small, shallow wells in the base of the petri dish. See ESI† Figure S6 for a detailed schematic.

HeLa cells were grown in DMEM (Gibco, Invitrogen, Oslo, Norway) supplanted with 10% FBS (Invitrogen) and 1% pen/strep and passaged regularly. Cells were seeded in the modified 35 mm dishes at a typical density of 20 000 cells/cm^2, i.e. 200 000 cells per dish. For live cell imaging cells were labelled with 1 µM calcein-AM (Invitrogen) and Hoechst 34580 in complete DMEM for 30 minutes. The media was then changed to Leibovitz L-15, a CO_2 independent medium, and cells were imaged at 37 °C.

For fixed cell experiments, cells were fixed in 4% paraformaldehyde in PBS. Cells were then labelled with CellMask Orange (Invitrogen), Hoechst 34580, or permeabilized for 3 minutes in 0.1% Triton X-100 and labelled with phalloidin-Alexa488 (Invitrogen). For 3D-SIM experiments, cells were mounted in Vectashield, while for confocal and

STED experiments cells were mounted in Mowiol with 0.05% PPD.

As CellMask Orange does not survive cell permeabilization, in experiments where both the membrane and actin was visualized the cells were fixed, labelled with CellMask and imaged, before permeabilizing and labelling actin. The same cells were re-located on the sample and the images were automatically overlayed using the StackReg plugin [70] for FIJI.

Cell imaging

Live and fixed HeLa cells were imaged using a Leica SP8 or SP5 confocal microscope either with a 10X 0.4NA air objective or a 63X 1.4NA oil objective, a Zeiss Axio Observer Z1 TIRF with a 100X 1.4NA oil objective and a Andor iXon DU 897-BV EMCCD camera, a OMX V4 Blaze 3D-SIM microscope with a 100X 1.45NA oil objective and a Leica SP8 confocal microscope with a 592 nm STED depletion laser and a 100X 1.4NA oil objective. High resolution confocal images or stacks were acquired with a 70 nm pixel size and 200 nm slice spacing, TIRF images were acquired at 100 nm pixel size, 3D-SIM images were acquired at 80 nm pixel size with 120 nm slice spacing. STED images were acquired at system optimized pixel size, typically 20-30 nm in XY and 80-100 nm i Z. 3D-SIM images were deconvoluted using software supplied with the microscope, and STED images were deconvoluted using Huygens Professional.

Cell images were prepared using FIJI. Automated analysis of cell viability and cell shape was performed using CellProfiler [71]. For cells on nanopillars, 6 parallel samples were analysed, for a total of over 3600 cells (at least 600 cells for each condition, 4 different nanopillar spacings and 2 control areas). For cells on nanolines, 3 parallel samples were analysed, for a total of over 1800 cells. TIRF and widefield images were inspected manually, at least 25 cells per nanopillar spacing (spacings of 1 µm, 2 µm, 5 µm and 10 µm) were investigated, for a total of 120 analysed cells..

Acknowledgements

For access to the TIRF instrument we would like to thank Prof. B.T. Stokke and the Reasearch council of Norway (183338/S10). For assistance with 3D-SIM imaging, we thank V. Sørensen at the Core facility for Advanced Light Microscopy at the Oslo University Hospital. STED imaging was performed at the Cellular and Molecular Imaging Core Facility, Norwegian University of Science and Technology (NTNU), with the aid of B. Sporsheim. The Research Council of Norway is acknowledged for the support to the Norwegian Micro- and Nano-Fabrication Facility, NorFab (197411/V30). K.S.B. is additionally supported by grants from NTNU and the Norwegian PhD-school in Medical Imaging.

References

1 M. M. Stevens and J. H. George, *Science*, 2005, **310**, 1135–8.
2 N. D. Gallant, J. L. Charest, W. P. King and A. J. García, *J. Nanosci. Nanotechnol.*, 2007, **7**, 803–7.
3 C. J. Bettinger, R. Langer and J. T. Borenstein, *Angew. Chem. Int. Ed. Engl.*, 2009, **48**, 5406–15.
4 H. V. Unadkat, M. Hulsman, K. Cornelissen, B. J. Papenburg, R. K. Truckenmüller, A. E. Carpenter, M. Wessling, G. F. Post, M. Uetz, M. J. T. Reinders, D. Stamatialis, C. A. van Blitterswijk and J. de Boer, *Proc. Natl. Acad. Sci. U. S. A.*, 2011, **108**, 16565–70.
5 J. Y. Lim and H. J. Donahue, *Tissue Eng.*, 2007, **13**, 1879–91.
6 S. Bonde, N. Buch-Må nson, K. R. Rostgaard, T. K. Andersen, T. Berthing and K. L. Martinez, *Nanotechnology*, 2014, **25**, 362001.
7 R. Elnathan, M. Kwiat, F. Patolsky and N. H. Voelcker, *Nano Today*, 2014, **9**, 172–196.
8 F. Mumm, K. M. Beckwith, S. Bonde, K. L. Martinez and P. Sikorski, *Small*, 2013, **9**, 263–72.
9 S. Bonde, T. Berthing, M. H. Madsen, T. K. Andersen, N. Buch-Må nson, L. Guo, X. Li, F. Badique, K. Anselme, J. Nygå rd and K. L. Martinez, *ACS Appl. Mater. Interfaces*, 2013, **5**, 10510–9.
10 L. Hanson, Z. C. Lin, C. Xie, Y. Cui and B. Cui, *Nano Lett.*, 2012, **12**, 5815–20.
11 Z. Yu, T. E. McKnight, M. N. Ericson, A. V. Melechko, M. L. Simpson and B. Morrison, *Nano Lett.*, 2007, **7**, 2188–95.
12 C. Xie, Z. Lin, L. Hanson, Y. Cui and B. Cui, *Nat. Nanotechnol.*, 2012, **7**, 185–90.
13 J. T. Robinson, M. Jorgolli, A. K. Shalek, M.-H. Yoon, R. S. Gertner and H. Park, *Nat. Nanotechnol.*, 2012, **7**, 180–4.
14 W. Hällström, M. Lexholm, D. B. Suyatin, G. Hammarin, D. Hessman, L. Samuelson, L. Montelius, M. Kanje and C. N. Prinz, *Nano Lett.*, 2010, **10**, 782–7.
15 C. Xie, L. Hanson, W. Xie, Z. Lin, B. Cui and Y. Cui, *Nano Lett.*, 2010, **10**, 4020–4.
16 S. Y. Kim and E. G. Yang, *Nanotechnology*, 2013, **24**, 455704.
17 H. Persson, C. Kø bler, K. Mø lhave, L. Samuelson, J. O. Tegenfeldt, S. Oredsson and C. N. Prinz, *Small*, 2013, **9**, 4006–16.
18 M. a. Bucaro, Y. Vasquez, B. D. Hatton and J. Aizenberg, *ACS Nano*, 2012, **6**, 6222–30.
19 J. Padmanabhan, E. R. Kinser, M. A. Stalter, C. Duncan-Lewis, J. L. Balestrini, A. J. Sawyer, J. Schroers and T. R. Kyriakides, *ACS Nano*, 2014, **8**, 4366–75.
20 S. T. Kim, D.-J. Kim, T.-J. Kim, D.-W. Seo, T.-H. Kim, S.-Y. Lee, K. Kim, K.-M. Lee and S.-K. Lee, *Nano Lett.*, 2010, **10**, 2877–83.
21 S.-K. Lee, G.-S. Kim, Y. Wu, D.-J. Kim, Y. Lu, M. Kwak, L. Han, J.-H. Hyung, J.-K. Seol, C. Sander, A. Gonzalez, J. Li and R. Fan, *Nano Lett.*, 2012, **12**, 2697–704.
22 W. Kim, J. K. Ng, M. E. Kunitake, B. R. Conklin and P. Yang, *J. Am. Chem. Soc.*, 2007, **129**, 7228–7229.
23 T. E. McKnight, A. V. Melechko, D. K. Hensley, D. G. J. Mann, G. D. Griffin and M. L. Simpson, *Nano Lett.*, 2004, **4**, 1213–1219.
24 A. K. Shalek, J. T. Robinson, E. S. Karp, J. S. Lee, D.-R. Ahn, M.-H. Yoon, A. Sutton, M. Jorgolli, R. S. Gertner, T. S. Gujral, G. MacBeath, E. G. Yang and H. Park, *Proc. Natl. Acad. Sci. U. S. A.*, 2010, **107**, 1870–5.
25 L. Lampert, B. Timonen, S. Smith, B. Davidge, H. Li, J. F. Conley, J. D. Singer and J. Jiao, *Chem. Commun.*, 2014, **50**, 1234–7.
26 J. Yang, F. R. J. Rose, N. Gadegaard and M. R. Alexander, *Adv. Mater.*, 2009, **21**, 300–304.
27 E. H. Ahn, Y. Kim, Kshitiz, S. S. An, J. Afzal, S. Lee, M. Kwak, K.-Y. Suh, D.-H. Kim and A. Levchenko, *Biomaterials*, 2014, **35**, 2401–10.
28 H. Lorenz, M. Despont, N. Fahrni, N. LaBianca, P. Renaud and P. Vettiger, *J. Micromechanics Microengineering*, 1997, **7**, 121–124.

29 A. Pepin, V. Studer, D. Decanini and Y. Chen, *Microelectron. Eng.*, 2004, **73**, 233–237.

30 D. López-Romero, C. Barrios, M. Holgado, M. Laguna and R. Casquel, *Microelectron. Eng.*, 2010, **87**, 663–667.

31 F. J. Ortega, M.-J. Bañuls, F. J. Sanza, R. Casquel, M. F. Laguna, M. Holgado, D. López-Romero, C. a. Barrios, A. Maquieira and R. Puchades, *Biosensors*, 2012, **2**, 291–304.

32 C.-W. Kuo, J.-Y. Shiu, F.-C. Chien, S.-M. Tsai, D.-Y. Chueh and P. Chen, *Electrophoresis*, 2010, **31**, 3152–3158.

33 V. N. Vernekar, D. K. Cullen, N. Fogleman, Y. Choi, A. J. García, M. G. Allen, G. J. Brewer and M. C. LaPlaca, *J. Biomed. Mater. Res. A*, 2009, **89**, 138–51.

34 M. Stangegaard, Z. Wang, J. P. Kutter, M. Dufva and A. Wolff, *Mol. Biosyst.*, 2006, **2**, 421.

35 P. Y. Yeh, Z. Zhang, M. Lin and X. Cao, *Langmuir*, 2012, **28**, 16227–36.

36 S. L. Tao, K. Popat and T. a. Desai, *Nat. Protoc.*, 2006, **1**, 3153–8.

37 Y. Wang, M. Bachman, C. E. Sims, G. P. Li and N. L. Allbritton, *Langmuir*, 2006, **22**, 2719–2725.

38 F. Walther, P. Davydovskaya, S. Zürcher, M. Kaiser, H. Herberg, A. M. Gigler and R. W. Stark, *J. Micromechanics Microengineering*, 2007, **17**, 524–531.

39 P. Xue, J. Bao, Y. J. Chuah, N. V. Menon, Y. Zhang and Y. Kang, *Langmuir*, 2014, **30**, 3110–7.

40 L. Shechter, J. Wynstra and R. P. Kurkjy, *Ind. Eng. Chem.*, 1956, **48**, 94–97.

41 S. De and A. Khan, *Chem. Commun.*, 2012, **48**, 3130–2.

42 C. E. Hoyle, A. B. Lowe and C. N. Bowman, *Chem. Soc. Rev.*, 2010, **39**, 1355–87.

43 E. Peris, M.-J. Bañuls, R. Puchades and A. Maquieira, *J. Mater. Chem. B*, 2013, **1**, 6245.

44 L. De Sio, J. G. Cuennet, A. E. Vasdekis and D. Psaltis, *Appl. Phys. Lett.*, 2010, **96**, 131112.

45 A. Marino, G. Ciofani, C. Filippeschi, M. Pellegrino, M. Pellegrini, P. Orsini, M. Pasqualetti, V. Mattoli and B. Mazzolai, *ACS Appl. Mater. Interfaces*, 2013, **5**, 13012–21.

46 B. L. Aekbote, J. Jacak, G. J. Schütz, E. Csányi, Z. Szegletes, P. Ormos and L. Kelemen, *Eur. Polym. J.*, 2012, **48**, 1745–1754.

47 R. Liu, B. Lu, S. Xie, J. Wan, Z. Shu, X. Qu and Y. Chen, 2009, **55**, 1290–1294.

48 B. Thierry, M. Jasieniak, L. C. P. M. de Smet, K. Vasilev and H. J. Griesser, *Langmuir*, 2008, **24**, 10187–95.

49 J. F. Joanny and P. G. de Gennes, *J. Chem. Phys.*, 1984, **81**, 552.

50 M. Wirde, U. Gelius and L. Nyholm, *Langmuir*, 1999, **15**, 6370–6378.

51 J. Escorihuela, M.-J. Bañuls, R. Puchades and A. Maquieira, *Bioconjug. Chem.*, 2012, **23**, 2121–8.

52 G. Csucs, R. Michel, J. W. Lussi, M. Textor and G. Danuser, *Biomaterials*, 2003, **24**, 1713–20.

53 M. Hennemeyer, F. Walther, S. Kerstan, K. Schürzinger, A. M. Gigler and R. W. Stark, *Microelectron. Eng.*, 2008, **85**, 1298–1301.

54 W. Hu, A. S. Crouch, D. Miller, M. Aryal and K. J. Luebke, *Nanotechnology*, 2010, **21**, 385301.

55 C. Oakley and D. Brunette, *J. Cell Sci.*, 1993, **106**, 343–354.

56 W. Hällström, T. Må rtensson, C. Prinz, P. Gustavsson, L. Montelius, L. Samuelson and M. Kanje, *Nano Lett.*, 2007, **7**, 2960–5.

57 X. Xie, A. M. Xu, M. R. Angle, N. Tayebi, P. Verma and N. A. Melosh, *Nano Lett.*, 2013, **13**, 6002–8.

58 S. Wang, Y. Wan and Y. Liu, *Nanoscale*, 2014, **6**, 12482–9.

59 T. Berthing, S. Bonde, K. R. Rostgaard, M. H. Madsen, C. B. Sø rensen, J. Nygå rd and K. L. Martinez, *Nanotechnology*, 2012, **23**, 415102.

60 K. R. Rostgaard, R. S. Frederiksen, Y.-C. C. Liu, T. Berthing, M. H. Madsen, J. Holm, J. Nygå rd and K. L. Martinez, *Nanoscale*, 2013, **5**, 10226–35.

61 H. T. McMahon and J. L. Gallop, *Nature*, 2005, **438**, 590–6.

62 J. Albuschies and V. Vogel, *Sci. Rep.*, 2013, **3**, 1658.

63 J. Peng, M. A. Garcia, J.-S. Choi, L. Zhao, K.-J. Chen, J. R. Bernstein, P. Peyda, Y.-S. Hsiao, K. W. Liu, W.-Y. Lin, A. D. Pyle, H. Wang, S. Hou and H.-R. Tseng, *ACS Nano*, 2014, **8**, 4621–9.

64 D. Drouin, A. R. Couture, D. Joly, X. Tastet, V. Aimez and R. Gauvin, *Scanning*, 2007, **29**, 92–101.

65 R. Stevens, L. Stevens and N. Price, *Biochem. Educ.*, 1983, **11**, 70.

66 A. F. Stalder, T. Melchior, M. Müller, D. Sage, T. Blu and M. Unser, *Colloids Surfaces A Physicochem. Eng. Asp.*, 2010, **364**, 72–81.

67 J. Schindelin, I. Arganda-Carreras, E. Frise, V. Kaynig, M. Longair, T. Pietzsch, S. Preibisch, C. Rueden, S. Saalfeld, B. Schmid, J.-Y. Tinevez, D. J. White, V. Hartenstein, K. Eliceiri, P. Tomancak and A. Cardona, *Nat Methods*, 2012, **9**, 676–682.

68 K. M. Beckwith and P. Sikorski, *Biofabrication*, 2013, **5**, 045009.

69 A. Azioune, M. Storch, M. Bornens, M. Théry and M. Piel, *Lab Chip*, 2009, **9**, 1640–2.

70 P. Thévenaz, U. E. Ruttimann and M. Unser, *IEEE Trans. Image Process.*, 1998, **7**, 27–41.

71 L. Kamentsky, T. R. Jones, A. Fraser, M.-A. Bray, D. J. Logan, K. L. Madden, V. Ljosa, C. Rueden, K. W. Eliceiri and A. E. Carpenter, *Bioinformatics*, 2011, **27**, 1179–80.